

UKAEA-CCFE-CP(21)08

C J Ham, A Bokshi, D Brunetti, G Bustos Ramirez, B
Chapman, J W Connor, D Dickinson, A R Field, J P
Graves, T Kiviniemi, S Leerink, B McMillan, S
Newton, S Pamela, C M Roach, S Saarelma, J
Simpson, S F Smith, P Strand, A Virtanen, the JET

Contributors*

Understanding reactor relevant tokamak pedestals

This document is intended for publication in the open literature. It is made available on the understanding that it may not be further circulated and extracts or references may not be published prior to publication of the original when applicable, or without the consent of the UKAEA Publications Officer, Culham Science Centre, Building K1/O/83, Abingdon, Oxfordshire, OX14 3DB, UK.

Enquiries about copyright and reproduction should in the first instance be addressed to the UKAEA Publications Officer, Culham Science Centre, Building K1/O/83 Abingdon, Oxfordshire, OX14 3DB, UK. The United Kingdom Atomic Energy Authority is the copyright holder.

The contents of this document and all other UKAEA Preprints, Reports and Conference Papers are available to view online free at scientific-publications.ukaea.uk/

Understanding reactor relevant tokamak pedestals

C J Ham, A Bokshi, D Brunetti, G Bustos Ramirez, B Chapman, J W Connor, D Dickinson, A R Field, J P Graves, T Kiviniemi, S Leerink, B McMillan, S Newton, S Pamela, C M Roach, S Saarelma, J Simpson, S F Smith, P Strand, A Virtanen, the JET Contributors*

Understanding reactor relevant tokamak pedestals

C J Ham¹, A Bokshi², D Brunetti¹, G Bustos Ramirez³, B Chapman¹, J W Connor¹, D Dickinson⁴, A R Field¹, L Frassinetti⁵, A Gillgren⁹, J P Graves³, T P Kiviniemi⁶, S Leerink⁶, B McMillan⁷, S Newton¹, S Pamela¹, C M Roach¹, S Saarelma¹, J Simpson¹, S F Smith¹, E R Solano⁸, P Strand⁹, A J Virtanen⁶ and the JET Contributors*

¹UKAEA-CCFE, Culham Science Centre, Abingdon, Oxon, OX14 3DB, UK; ²Institute for Plasma Research, Gandhinagar, India; ³EPFL, Swiss Plasma Center, CH-1015 Lausanne, Switzerland; ⁴York Plasma Institute, University of York, Heslington, York YO10 5DD, UK; ⁵Division of Fusion Plasma Physics, KTH, Stockholm SE; ⁶Aalto University, FI-00076 Aalto, Finland; ⁷University of Warwick, Coventry CV4 7AL, UK; ⁸Laboratorio Nacional de Fusin, CIEMAT, Madrid, Spain; ⁹Chalmers University of Technology, SE-412 96 Gothenburg, Sweden; *See author list of E. Joffrin et al., Nucl. Fusion 59 112021 (2019)

E-mail: christopher.ham@ukaea.uk

Abstract. The physics of the tokamak pedestal is still not fully understood. However, this will be a key element for improving our confidence in designing potential fusion power plants. There is no fully predictive model for the pedestal height and width for example. Work has been carried out as part of a collaboration on reactor relevant pedestal physics. We report here some of the results and also review some of the wider work which will be reported in full elsewhere. First, we attempt to use a gyrokinetic-based calculation to eliminate the pedestal top density as a model input for Europed/EPED pedestal predictions. We assume power balance at the top of the pedestal, that is, the heat flux crossing the separatrix must be equal to the heat source at the top of the pedestal and investigate the consequences of this assumption. Unfortunately, this method was not successful. Second, we investigate the effects of non flux surface density on the bootstrap current. Third, type I ELMs will not be tolerable for a reactor relevant regime due to the damage that they are expected to cause to plasma facing components. In recent years various methods of running tokamak plasmas without large ELMs have been developed. These include small and no ELM regimes, the use of resonant magnetic perturbations and the use of vertical kicks. We discuss the quiescent H-mode here. Finally we give directions for future work.

Submitted to: *Plasma Phys. Control. Fusion*

1. Introduction

1.1. Background

The pedestal, which is associated with a local formation of a transport barrier (in energy and particles), plays an important role in determining the confinement in tokamak H-mode plasmas. Indeed the increased confinement associated with the steep pedestal gradients strongly affect the global plasma performance, and the expected fusion power associated with a given scenario. However, the steep pressure gradients in this transport barrier also lead to edge localized modes (ELMs) [1]. There is a reasonable understanding of the pedestal in type I ELM regimes being limited by ideal MHD peeling-ballooning modes. The EPED model can predict pedestal height and width of type I ELMing plasmas on current machines given various assumptions [2], however, type I ELMs are known to damage plasma facing components and so future large tokamaks must operate with small or no ELMs. Our collaboration aimed to understand various aspects of the physics of reactor relevant pedestals. We document some of the new results here and review the work that will appear in detail elsewhere. There is still much to understand and we will give our thoughts on where future efforts could be directed.

1.2. Overview

In Section 2 we review recent work, especially that carried out as part of our collaboration, which improves our understanding of pedestal physics which is relevant to reactors. In Section 3 we describe the work we have done on improving pedestal prediction models. In particular, making the EUROPED model [3] more general and building our understanding of the physics that underlies the model. In Section 4 we investigate how a non flux surface density, i.e. density is not constant on a flux surface, may change the bootstrap current. In Section 5 we discuss the improvements we have made in our understanding of the QH mode. We finish with a summary and directions for future work in Section 6.

2. Recent work on Reactor Relevant Pedestals

The pedestal continues to be a rich source of interesting physics and we still do not have a solid understanding of the underlying processes. It is important that we develop our understanding of the pedestal not just because of the interesting physics but also because to design and build future tokamak fusion reactors we must be able to predict pedestals to give confidence that potential designs will operate at the required performance.

The EPED and EUROPED models have had some success in this area but they have underlying assumptions that to one degree or another are based on experimental observations. One such assumption is the pedestal gradient being limited by the $\sqrt{\beta_{pol}}$. This is an assumption about the transport and the instabilities that are assumed to produce that transport. We report work in Section 3 that seeks to improve our approach in this area.

A further important part of the physics of the pedestal is the bootstrap current that is generated by the steep pressure gradient in the pedestal region. There are various ways

38 of calculating the bootstrap current that involve either direct solution of the neoclassical
39 equations [4, 5] or a fitting of the numerical solution over various parameter ranges [6], [7].
40 Members of our collaboration have used the global full f gyrokinetic code ELMFIRE [8]
41 first to benchmark the Hager and Sauter models [9]. It was found that these two formulae
42 agree with ELMFIRE in the regime where there is no Shafranov Shift and low collisionality,
43 which is relevant for ELMFIRE. Further, ELMFIRE has been used to assess the effect of
44 poloidal variation of density on the bootstrap current [9]. Initial results indicate that there is
45 an effect which should be investigated further. Analytic calculations of the effect of poloidal
46 variation of density have been carried out and this analysis is presented in Section 4. We
47 have also investigated the effect of poloidal variation of density on MHD stability using the
48 JOREK code [10]. The initial results showed that the growth rate of low toroidal mode number
49 instabilities were affected but further work is required to confirm this.

50 Integrating all of the pedestal models together and running them could be quite time
51 consuming if the pedestal prediction is part of a design loop for a reactor design or to design a
52 shot or indeed to interpret experimental results. Members of our collaboration have therefore
53 been investigating the use of neural networks. These neural networks can be trained either on
54 experimental data or on the results of modelling and the resulting neural network can then be
55 used to produce fast pedestal predictions. This has been completed for JET using PENN [11].

56 Our collaboration investigated some of the small and no ELM regimes that will have to
57 be considered for a reactor. The quiescent H-mode (QH-mode) is one such ELM free regime
58 that has been investigated in DIII-D [12], JET [13] and at AUG [14]. The plasma still has a
59 pedestal and so has reactor relevant performance but it develops an edge harmonic oscillation
60 (EHO) which is thought to be a saturated MHD mode. This is thought to produce sufficient
61 density transport such that the peeling ballooning (PB) mode boundary is not reached and
62 so the ELM is avoided. Experimental evidence so far suggests that an edge rotation shear is
63 required for the QH-mode to appear. Our collaboration has investigated the QH-mode both
64 numerically and analytically. We have used the VMEC code to find saturated nonlinear MHD
65 states [15]. These can be found in two regimes. One where the safety factor profile (q profile)
66 is just below a rational at the plasma edge. This is the classical external kink mode. The other
67 is a pressure driven mode that requires a flattening of the q profile at the edge. This flattening
68 is provided by the bootstrap current which is driven by the pressure gradient in the pedestal.
69 The ballooning stability of these two saturated instabilities is discussed in Section 5. The
70 QH-mode in JET has also been investigated and in particular the effect of collisionality [16].
71 A model for Grassy ELMs has been investigated using a gyrofluid model implemented in the
72 BOUT++ framework. Initial tests of the model have been completed but further work will be
73 required to test it in the appropriate regime. An analytic model of type III ELMs has been
74 developed based on a resistive MHD model and this will be discussed elsewhere [17].

75 3. Pedestal Prediction

76 In this Section we seek to improve the well known EPED model. This model has various
77 assumptions underlying it. In particular, one input is the density at the pedestal top. We aim

78 here to use a gyrokinetic-based calculation to eliminate this input. This idea is to assume
 79 power balance at the top of the pedestal, that is, the heat flux crossing the separatrix must be
 80 equal to the heat source at the top of the pedestal. The workflow is as follows: use *Europed*
 81 with a range of $n_{e,ped}$ as input to get a corresponding range of $T_{e,ped}$; use a gyrokinetic-based
 82 calculation to test each pair of profiles and calculate the heat flux Q_{ped} and; then the pedestal
 83 prediction is the n_e, T_e profile pair with Q_{ped} equal to the experimental heat flux.

84 A key part is to calculate the heat flux. There are a number of options available
 85 which include: full, multi-scale gyrokinetic simulations including neoclassical terms; a
 86 trio of gyrokinetic simulations: nonlinear global ion-scale, nonlinear local electron-scale,
 87 neoclassical; quasilinear model with linear gyrokinetic simulations; quasilinear model with
 88 eigensolver e.g. QuaLiKiz [18] and finally; fast Neural network-type software trained on any
 89 of the above.

90 Work is underway to develop a sophisticated quasilinear model in the pedestal. At the
 91 time of writing a comprehensive quasilinear model that can be used reliably and routinely has
 92 not been published. To match the heat flux we must therefore run fully non-linear simulations
 93 that capture the spatial and temporal scales of the turbulence believed to be the primary source
 94 of heat flux through the pedestal. However, the computational expense of such simulations is
 95 prohibitive. We therefore opt for a comparison to linear spectra instead. As we shall see, it is
 96 unlikely that further information would be obtained from nonlinear simulations.

97 In order to test the heat flux matching concept we examine JET-ILW pulse #84793
 98 which lies along the peeling-ballooning stability boundary, Fig. 1 [19], and therefore satisfies
 99 one of the key EPED model assumptions. We start by assuming slab-ETG modes are the
 100 primary driver of turbulent heat flux, and neglect neoclassical heat flux, which can easily be
 101 added to the model later. We use the GENE gyrokinetic code [20, 21] in its local model
 102 of operation. The resolution requirements for this pulse are known from previous analysis.
 103 Before continuing, it is first necessary to test the validity of the EPED model and discuss some
 104 of the features and extensions of *Europed* that are required in order to fulfil our objective.

105 3.1. *Europed* results

106 3.1.1. *Details of the EPED model and Europed package* The two principle assumptions
 107 of the EPED1 model are: a) an ideal-MHD constraint - the pedestal is limited by Peeling-
 108 Ballooning modes, and b) a transport constraint - the width of the pressure pedestal scales
 109 with the square-root of the pedestal poloidal beta according to: $\Delta_p = C\beta_{p,ped}^{1/2}$; where C is a
 110 model constant. The two main inputs to the EPED model are the global beta β_N or β_p , and
 111 the value of density at the pedestal top $n_{e,ped}$. In addition, the standard EPED1 model has the
 112 following fixed assumptions: $\Delta_p = \Delta_{T_e} = \Delta_{n_e}$; the density and temperature profiles are aligned
 113 to the same pedestal position; the profiles are well described by a mtanh fit; and $T_i = T_e$.

114 EPED1 also has three notable variable assumptions which are usually device specific:
 115 the transport constraint model constant $C = 0.076$; $T_{e,sep} = 100\text{eV}$ for JET-ILW [22, 23] and;
 116 $n_{e,sep} = f \times n_{e,ped}$ where f is a constant - we often use $f = 0.25$.

117 The value of the model constant C can be obtained from an empirical fit to experimental

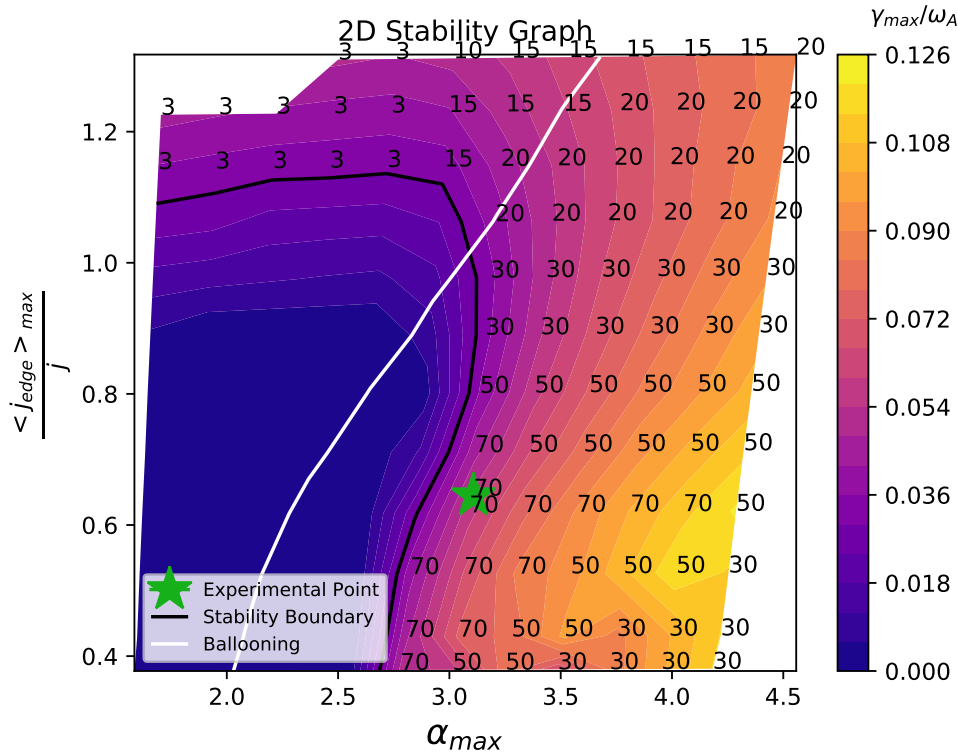


Figure 1. Linear MHD pedestal stability analysis for the deuterium plasma #84793, $I_p = 1.4MA$, $B_t = 1.7T$. The numbers indicate the most unstable mode number at given edge current and pressure gradient.

118 data. The value of $T_{e,sep}$ is device specific but in the case of JET-ILW, this is borne out
 119 well by edge modelling. The relationship $n_{e,sep}/n_{e,ped} = 1/4$ is less well-founded, but the
 120 pressure profile prediction from EPED1 appears to be relatively insensitive to this. As we
 121 shall see later, the choice of $n_{e,sep}$ may have important consequences for the stability of slab-
 122 like microinstabilities in the pedestal. In practice, the density peaking factor, related to the
 123 core density, must also be specified. However, pedestal predictions are mostly insensitive to
 124 this so we omit it from discussion here. The Europed package consists of the EPED series of
 125 models along with some additional functionality. Chief among these are several models for
 126 the self-consistent heating in the core which allow for an arbitrary core profile shape; and two
 127 models which allow us to specify $n_{e,ped}$ [24]. These models are not the subject of this work
 128 and we will be running Europed in the beta constrained mode of operation with $n_{e,ped}$ specified
 129 according to our model. There are two extensions of the EPED model within Europed that
 130 are critical for the heat flux matching concept discussed in the following. The first is the
 131 ability to specify a relative shift, δ_{n-T} , between the density and temperature pedestals, an
 132 important feature of JET-ILW pedestals [23]. The second is the possibility of specifying the
 133 ratio $\Delta T_e/\Delta n_e$, which was implemented as part of this project.

134 *3.1.2. Europed runs - the effect of $\Delta_{T_e} \neq \Delta_{n_e}$ and $\delta_{n-T} \neq 0$* It is well known that an important
 135 parameter related to the linear stability of slab-ETG modes is the ratio of the normalised
 136 density and temperature scale lengths η_e given by:

$$\eta_e = \frac{d\ln(T_e)}{d\ln(n_e)} = \frac{n_e \nabla T_e}{T_e \nabla n_e} = \frac{1/L_{T_e}}{1/L_{n_e}} = \frac{L_{n_e}}{L_{T_e}}. \quad (1)$$

137 Previous work by F. Jenko and others has shown that strong linear slab-ETG drive
 138 requires $\eta_e \gtrsim 1$ [20]. The standard EPED assumptions that the temperature and density
 139 pedestal positions, henceforth referred to as Ψ_{N,T_e} and Ψ_{N,n_e} respectively, are aligned, and the
 140 pedestal widths Δ_{T_e} and Δ_{n_e} are equal, mean that $\eta_e \approx 1$ across the pedestal region by design.
 141 To this end, we explore the consequences of a finite relative shift $\delta_{n-T} = \Psi_{N,n_e} - \Psi_{N,T_e} \neq 0$
 142 and $\Delta_{T_e} \neq \Delta_{n_e}$ on Europed predictions for JET-ILW pulse #84793. Figure 2 shows the
 143 experimental profiles in dotted black along with the results of four Europed runs. Dashed lines
 144 correspond to $\delta_{n-T} = 0$ whereas solid lines correspond to $\delta_{n-T} = 0.8\%$. Blue lines denote the
 145 default EPED assumption $\Delta_{T_e}/\Delta_{n_e} = 1$ while red lines show the results in which $\Delta_{T_e}/\Delta_{n_e} =$
 146 1.76 (chosen to match experiment), made possible by newly implemented functionality. Note
 147 that a corollary of the latter input is that $\Delta_{n_e} < \Delta_{p_e} < \Delta_{T_e}$ [25]

148

149 In all four cases, the predicted Δ_p varied between ~ 0.030 and 0.034 , i.e. Δ_p is
 150 relatively insensitive to these modifications between the relationship between the density and
 151 temperature pedestals. We also note in passing that the Europed predicted Δ_p is approximately
 152 equal to the experimental Δ_{n_e} , a feature that will be explored in future work with a larger
 153 experimental dataset. In these four runs we set $n_{e,sep} = 0.33n_{e,ped}$, which, in the case
 154 of a finite relative shift and equal density and temperature pedestal widths, matches the
 155 experiment almost exactly. This is because of the aforementioned, and perhaps coincidental,
 156 correspondence between the Europed predicted Δ_{n_e} and the experimental Δ_p . The solid traces
 157 show that, in general, δ_{n-T} influences pedestal profile prediction more than having $\Delta_{T_e} \neq \Delta_{n_e}$.
 158 The solid red line has the most physical effects in that δ_{n-T} and $\Delta_{T_e}/\Delta_{n_e}$ have been chosen to
 159 match experiment. This prediction therefore gives the closest match in $T_{e,ped}$ to experiment,
 160 but under-predicts the width of both the density and temperature pedestals. Note that this
 161 prediction required the input of two known quantities from experiment. Figure 3 displays:
 162 η_e , the normalised density gradient, and the normalised temperature gradient corresponding
 163 to the profiles shown in Fig. 2. The colour scheme and line-styles are the same as Fig. 2. The
 164 dashed blue line, corresponding to the standard EPED1 prediction, shows identical density
 165 and temperature gradients in the steep gradient region, along with a flat $\eta_e \sim 1$ trace. Looking
 166 at the solid blue line we see that the finite relative shift has flattened the density profile in
 167 the pedestal region ($\Psi_N \leq 1$) which results in a larger, and non-constant value of η_e more
 168 in line with experiment. In the dashed red line, with no relative shift but unequal pedestal
 169 widths, the Δ_{n_e} prediction has decreased which has realised in a normalised density gradient
 170 much larger than the experimental value. This has the effect of lowering η_e . However, as
 171 $\Delta_{T_e}/\Delta_{n_e} > 1$ means $\Delta_{T_e} > \Delta_p$, the normalised temperature gradient is less than that of the
 172 standard EPED1 prediction (dashed blue trace). These two effects, larger density gradient

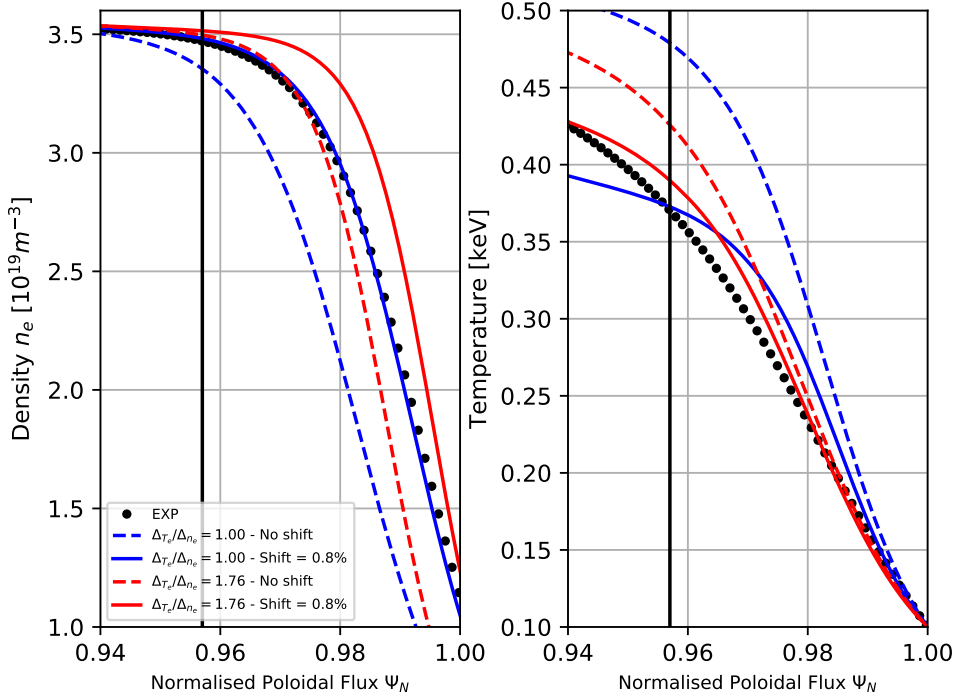


Figure 2. Density (left) and electron temperature (right) as a function of normalised Ψ_N in the pedestal region for JET-ILW pulse #84793. An mtanh fit to raw HRTS data is shown in black. Blue traces show Europed predictions with $\Delta T_e/\Delta n_e = 1.0$ (the default EPED assumption), while red traces show Europed predictions with $\Delta T_e/\Delta n_e = 1.76$ (the experimental value). Dashed traces show Europed predictions with $\delta_{n-T} = 0$ (the default EPED assumption), while red traces show Europed predictions with $\delta_{n-T} = 0.8\%$ (the experimental value). In both panels, the vertical black line denotes $\Psi_N \approx 0.956$, which is the location of the temperature pedestal top for the widest pedestal prediction. Europed data points with $\Psi_N \lesssim 0.956$ are therefore outside the range of accurate Europed predictions.

173 and smaller temperature gradient, compensate for each other and lead to an η_e profile which
 174 closely resembles the experimental profile. When we add a relative shift to this, shown in the
 175 solid red trace, the flat density profile increases η_e to larger values than experiment. Thus,
 176 despite having less physical effects, the dashed red trace seems to be a better predictor of
 177 η_e than the solid red trace. This is a coincidence, the normalised density gradient profile is
 178 clearly not in line with experiment.

179 3.2. Proof-of-principle test

180 We now proceed to test our heat flux matching idea for this pulse using our proxy method of
 181 comparing the linear spectra. Recall that the aim is to eliminate $n_{e,ped}$ as an input variable
 182 in the EPED model. Using the experimental values of $\delta_{n-T} = 0.8\%$ and $\Delta T_e/\Delta n_e = 1.76$, we
 183 perform a three point scan of $n_{e,ped}$ centred on the experimental value using: $3.0 \times 10^{19} m^{-3}$,
 184 $3.5 \times 10^{19} m^{-3}$, and $4.0 \times 10^{19} m^{-3}$. We again set $n_{e,sep} = 0.33 n_{e,ped}$. We have modified

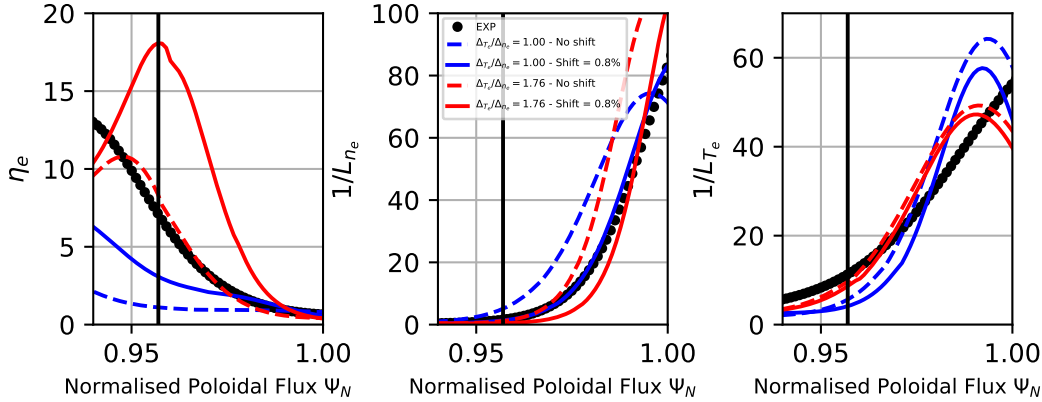


Figure 3. η_e (left), normalised density gradient (middle), and normalised temperature gradient (right) as a function of normalised Ψ_N in the pedestal region for JET-ILW pulse #84793. Experimental data is shown in black. Blue traces show Europed predictions with $\Delta T_e/\Delta n_e = 1.00$ (the default EPED assumption), while red traces show Europed predictions with $\Delta T_e/\Delta n_e = 1.76$ (the experimental value). Dashed traces show Europed predictions with $\delta_{n-T} = 0$ (the default EPED assumption), while solid traces show Europed predictions with $\delta_{n-T} = 0.8\%$ (the experimental value). In both panels, the vertical black line denotes $\Psi_N \approx 0.956$, which is the location of the temperature pedestal top for the widest pedestal prediction. Europed data points with $\Psi_N \lesssim 0.956$ are therefore outside the range of accurate Europed predictions.

185 Europed so that once the pedestal profile has been predicted, the code runs an instance
 186 of HELENA followed by CHEASE to produce an eqdsk equilibrium file for use in GENE
 187 simulation for the prediction. The profiles that result from this scan are shown in Fig. 4 and
 188 a plot of η_e and the normalised gradients are shown in Fig. 5. We immediately see from the
 189 left panel of Fig. 4 that that Δn_e turns out to be approximately the same in all three cases.
 190 This is because the Europed Δ_p prediction is approximately the same, and the two widths are
 191 related to each other by a constant scale factor. A consequence of this is that $\beta_{p,ped} \propto \Delta_p^2$
 192 is approximately constant, which in turn means that as $n_{e,ped}$ increases, $T_{e,ped}$ decreases in
 193 a predictable fashion according to $\propto 1/n_{e,ped}$. As expected, the scan point closest to the
 194 experimental value (orange) predicts pedestals that are closest experiment (black).

195 Looking at the centre panel of Fig. 5, we see that the normalised density gradients are
 196 very-nearly the same for the three scan-points (they are minutely different due to differences in
 197 $n_{e,sep}$). This is because the Δn_e prediction is the same for all three runs and the un-normalised
 198 density gradient scales with the input $n_{e,ped}$. We also see that the normalised temperature
 199 gradients are of similar value across a wide range of the pedestal. The values of $1/L_{T_e}$ do
 200 change towards the separatrix, but this is a consequence of fixing $T_{e,sep} = 100\text{eV}$ for differing
 201 values of $T_{e,ped}$. The combined effect of these two things is that the η_e profiles in the pedestal
 202 region (to the right of the vertical black line) are indistinguishable.

203 Given the similarity of the η_e , a/L_{n_e} , and a/L_{T_e} profiles, we expect no substantial difference
 204 in the linear spectra and nonlinear flux for the three scanpoints. There may be some difference
 205 in the GENE spectra for simulations at $\Psi_N \sim 0.98$ if the excited modes are driven primarily
 206 by changes in a/L_{T_e} . As discussed, the changes in the a/L_{T_e} profiles $\Psi_N \sim 0.98$ are a

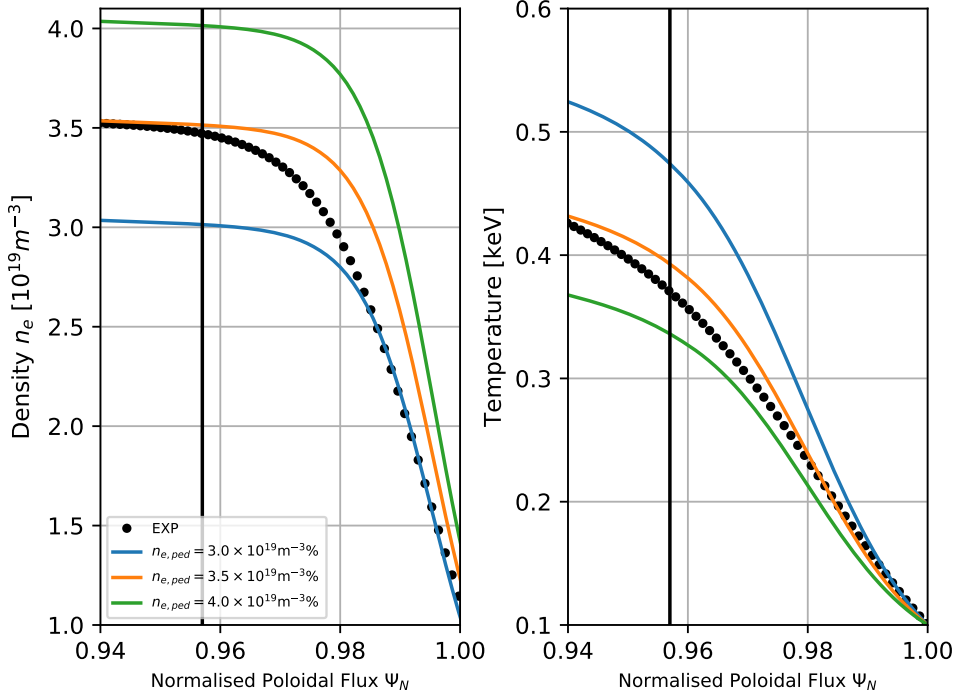


Figure 4. Density (left) and electron temperature (right) as a function of normalised Ψ_N in the pedestal region for JET-ILW pulse #84793. An mtanh fit to raw HRTS data is shown in black. Blue, orange, and green traces show Europed pedestal predictions using $3.0 \times 10^{19} m^{-3}$, $3.5 \times 10^{19} m^{-3}$, and $4.0 \times 10^{19} m^{-3}$ respectively. In both panels, the vertical black line denotes $\Psi_N \approx 0.956$, which is the location of the temperature pedestal top for the widest pedestal prediction. Europed data points with $\Psi_N \lesssim 0.956$ are therefore outside the range of accurate Europed predictions.

207 consequence of fixing $T_{e,sep} = 100\text{eV}$. For the moment, we assume this change in the a/L_{Te}
 208 profile has physical meaning and proceed to run a trio of linear local GENE simulations at
 209 $\rho_t = 0.98$ (in the vicinity of $\Psi_N \sim 0.98$). The resolution requirements for these simulations is
 210 known from previous work, and we restrict our attention to modes at the outboard mid-plane,
 211 that is $\theta_0 = 0$. Figure 6 shows the linear normalised growth rate γ as a function of the binormal
 212 wavenumber k_y . The red trace shows the equivalent calculation using the experimental profiles
 213 for this pulse. The modes present in the experimental profiles have a smaller peak γ than
 214 the spectra produced using the Europed predicted profiles predictions. More importantly,
 215 the growth rate spectra for the three Europed profile predictions are extremely similar. We
 216 emphasise that even these small variations in the spectra are almost entirely a consequence
 217 of fixing $T_{e,sep} = 100\text{eV}$. Past experience suggests that the nonlinear counterparts of linear
 218 simulations with extremely similar spectra will also predict extremely similar heat fluxes. We
 219 conclude that for this pulse, and this range of scanpoints, it is not possible to use gyrokinetic
 220 simulations as a means of eliminating $n_{e,ped}$ as an input variable.

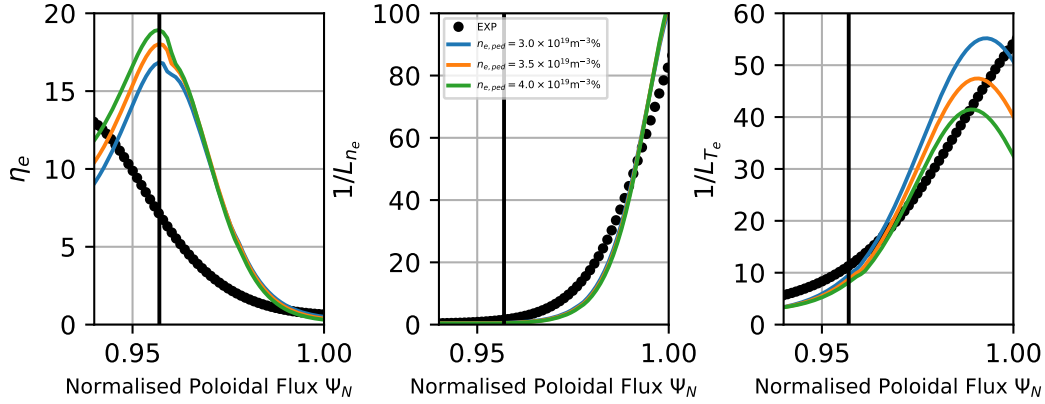


Figure 5. n_e (left), normalised density gradient (middle), and normalised temperature gradient (right) as a function of normalised Ψ_N in the pedestal region for JET-ILW pulse #84793. Experimental data is shown in black. Blue, orange, and green traces show Europed predictions using $3.0 \times 10^{19} m^{-3}$, $3.5 \times 10^{19} m^{-3}$, and $4.0 \times 10^{19} m^{-3}$ respectively. In both panels, the vertical black line denotes $\Psi_N \approx 0.956$, which is the location of the temperature pedestal top for the widest pedestal prediction. Europed data points with $\Psi_N \lesssim 0.956$ are therefore outside the range of accurate Europed predictions.

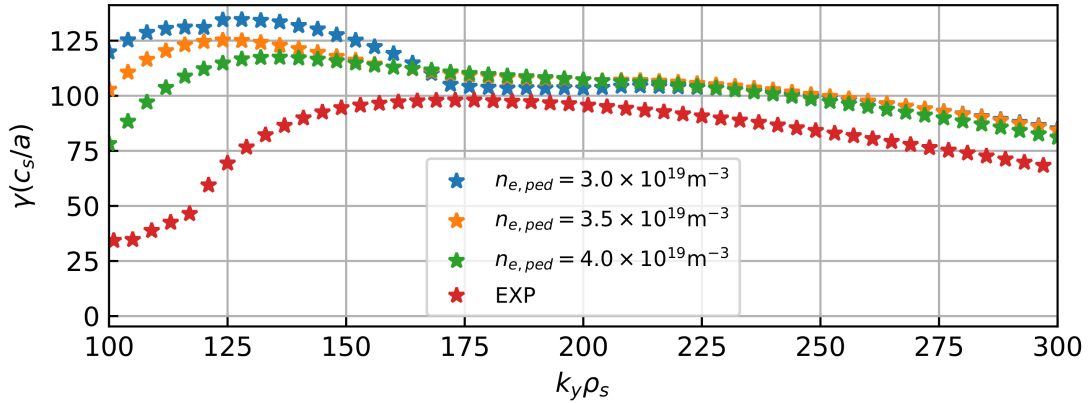


Figure 6. Growth rates as a function of binormal wavenumber k_y of slab-ETG modes from linear local GENE simulations at $\rho_t = 0.98$ for JET-ILW pulse #84793. The red trace corresponds to the experimental profiles at the same flux surface. Blue, orange, and green traces show Europed pedestal predictions using $3.0 \times 10^{19} m^{-3}$, $3.5 \times 10^{19} m^{-3}$, and $4.0 \times 10^{19} m^{-3}$ respectively.

221 3.3. Discussion

222 In this work we have tested the feasibility of using a gyrokinetic-based calculation as a means
 223 of eliminating the pedestal top density $n_{e,ped}$ as an input into the EPED/Europed model. Us-
 224 ing a JET-ILW pulse lying along the Peeling-Ballooning boundary as our test case, we found
 225 that in order for the Europed predictions to approach experiment the effects of relative shift
 226 $\delta_{n-T} = \Psi_{N,ne} - \Psi_{N,Te}$ and non-equal temperature and density pedestal widths had to be in-

cluded. We found that this was necessary in order to predict T_e and n_e profiles that have $\eta_e > 1$ and are hence susceptible to slab-ETG instabilities, which have been found to be important [26, 27]. In addition, we upgraded Europed to allow for $\Delta_{T_e}/\Delta_{n_e} \neq 1$ and to produce equilibrium files for use in gyrokinetic simulations. Note that these features allow us to predict profiles susceptible to slab-ITG instabilities as the EPED assumption $T_i = T_e$ results in $\eta_i = \eta_e$.

These additional physical effects aside, we found that for a range of $n_{e,ped}$ around the experimental value, the Europed predicted profiles were too similar for a linear gyrokinetic calculation to accurately distinguish between input profiles. We fully expect this result to carry over to a nonlinear calculation of heat flux, meaning it is currently not possible to use gyrokinetic simulations as a means of eliminating $n_{e,ped}$ as an input variable. The source of this limitation may lie within the EPED transport constraint $\Delta_p = C\beta_{p,ped}^{1/2}$. This relationship means that for a given shot, the predicted Δ_p and $\beta_{p,ped}$ will always be similar over a wide range of inputs. In evidence, a scan of δ_{n-T} from 0.4% to 1.1% (not shown here) resulted in a variation in the predicted Δ_p changes by only $\sim 9\%$. In the results discussed in previous sections, changing $\Delta_{T_e}/\Delta_{n_e}$ changed Δ_p by $\sim 4\%$ for $\delta_{n-T} = 0$ and by $\sim 13\%$ for $\delta_{n-T} = 0.8\%$. Most importantly, for the cursory $n_{e,ped}$ scan discussed above, Δ_p changed by only $\sim 5\%$. These small variations in $\Delta_p^2 \propto \beta_{p,ped} \propto T_{e,ped}$ mean that for an $n_{e,ped}$ scan, the normalised density and temperature gradients will always be similar, which in turn means the value of $\eta_e = \eta_i$ will always be similar.

In conclusion, using a gyrokinetic based calculation to eliminate $n_{e,ped}$ as an EPED/Europed input is not feasible until the transport assumption $\Delta = C\beta_{p,ped}^{1/2}$ is improved [28]. Such an improvement must be the primary focus of future work. Finally, we note that if $n_{e,ped}$ were known in advance, a gyrokinetic-based heat flux matching calculation may prove useful for eliminating the ratio $\Delta_{T_e}/\Delta_{n_e}$ and/or δ_{n-T} as model inputs, as Fig. 3 shows the driving parameters are much more sensitive to this.

4. Effect of a Poloidal Variation of the Plasma Density on the Bootstrap Current

The use of gas puffing and the result of recycling might be expected to introduce a poloidal variation of the plasma density on a flux surface [29] and it is of interest to investigate the impact this has on the bootstrap current [30] in a plasma H-mode edge pedestal, as it could affect the peeling-ballooning mode stability [31] believed to play a role in the triggering of ELMs in tokamak H-mode. Furthermore, toroidal rotation can also generate a variation in density, with it peaking on the outboard side [32].

We first describe the kinetic equation for a large aspect ratio tokamak geometry with a zero order (in a Larmor radius expansion) plasma distribution function that is a Maxwellian having a poloidally varying density, a model that we use to illustrate the calculation. Then we calculate the increment in the bootstrap current, relative to the standard result, that the poloidal variation in the density produces. However, it may well be that in reality the distribution differs from a simple Maxwellian and additional corrections to our simple model for the

bootstrap current might emerge, but these would involve a much more complex calculation. A related paper [33] avoided this difficulty by introducing a source (as a δ -function in poloidal angle) in the first order equation, rather than in lowest order as our Maxwellian ansatz implies. We compare the effect of sinusoidal variations in two situations: one up-down symmetric (case (a)), the other symmetric in the inboard-outboard direction (case (b)). In practice, however, edge modelling codes show the variation due to neutral sources crossing the separatrix may be better represented by a more poloidally localised function [34]. We therefore also consider case (c) where we represent this situation by a δ -function (although assuming the localisation exceeds the electron Larmor radius in order to justify the use of the electron drift kinetic equation in calculating the bootstrap current). We show this solution also serves as a Green's function for an arbitrary poloidal variation in density. Furthermore, it allows one to extend the calculation to describe a general, axisymmetric toroidal geometry although we limit this to toroidal equilibria with a small number of trapped particles to justify the use of the pitch-angle scattering collision operator - and also to up-down symmetric ones, for simplicity. The electron and ion temperatures will also respond to a density variation on a flux surface through rapid electron thermal transport along field lines and pressure equalisation on a flux surface on the sound time scale to produce temperature perturbations that equalises the plasma pressure on the surface. We consider the impact of this, as well as that of the density variation, on the incremental bootstrap current. A numerical investigation of this problem has been carried out using ELMFIRE [9]. Previous work on understanding the effect of a poloidal density variation on transport was carried out by Solano and Hazeltine [35]. This work is in the plateau regime rather than the banana regime and the structure of the source is different.

4.1. The model

The distribution function for species j , f_j , satisfies a kinetic equation

$$\frac{\partial f_j}{\partial t} + \frac{Iv_{\parallel}}{BR^2q} \frac{\partial f_j}{\partial \theta} - v_{dj} \cdot \nabla f_j + C_j(f_j) + S(r, \theta, v) = 0 \quad (2)$$

where spatial derivatives are at constant energy. In first order we introduce a source $S(r, \theta, v)$ to ensure a steady state if the drift terms lead to a net flux across a flux surface

Here we use velocity space co-ordinates: v , $\lambda = v_{\perp}^2/Bv^2$, $\sigma = v_{\parallel}/|v_{\parallel}|$, $v_{\parallel} = \sigma v \sqrt{(1 - \lambda B)}$ so that $\int d^3v = \pi \Sigma_{\sigma} \int B d\lambda \int v^2 dv / |\sqrt{(1 - \lambda B)}|$, $v_{dj} = (v_{\parallel}/B) \times \nabla(v_{\parallel}/\omega_{cj})$. Specialising to a large aspect ratio tokamak geometry and a steady state situation for simplicity (we indicate how to generalise our results to an arbitrary axisymmetric toroidal geometry later), this can be written [36]

$$\frac{v_{\parallel}}{Rq} \frac{\partial f_j}{\partial \theta} - \frac{m_j}{e_j} v_{\parallel} \left(\frac{\partial}{\partial r} \left(\frac{v_{\parallel}}{B} \right) \frac{\partial f_j}{r \partial \theta} - \frac{\partial}{r \partial \theta} \left(\frac{v_{\parallel}}{B} \right) \frac{\partial f_j}{\partial r} \right) + C_j(f_j) + S(r, \theta, v) = 0, \quad (3)$$

with $B = B_0(1 - \frac{r}{R} \cos \theta)$, so that $\frac{\partial}{\partial r}(v_{\parallel}/B) = -\frac{\cos \theta}{R}$ and $\frac{\partial}{\partial \theta}(v_{\parallel}/B) = \frac{\sin \theta}{R}$. We expand $f_j = F_{Mj} + f_{j1}$, where $F_{Mj}(v, r, \theta)$ is the Maxwellian and consider the incremental changes to f_j due to the effects of the perturbations, $\delta n_j(r, \theta)$ and $\delta T_j(r, \theta)$ in F_{Mj} .

To illustrate the calculational formalism, we just consider the effect of a density perturbation: $\delta n_j(r, \theta) = n_{0j}(r)\gamma_j(r)h_j(\theta)$, and assume a Lorentz collision model for the electrons [37]:

$$C_e(f_e) = v_{ei} \frac{v_{\parallel}}{v_{the}^2} \frac{\partial}{\partial \lambda} \left(\frac{v_{\parallel} \lambda}{B} \frac{\partial}{\partial \lambda} f_e \right) + v_{ei} \frac{v_{\parallel} u_{\parallel i}}{v_{the}^2} F_{Me}, \quad (4)$$

with $u_{\parallel i}$ the mean ion parallel flow. Since we ignore temperature gradients for the moment, the ion distribution is merely a displaced Maxwellian. To capture the effect of the $\delta T_j(r, \theta)$, it will be necessary to include an ion flow, like-particle collisions and the effects of the energy dependence of the collision frequencies [37]; including the former is discussed below and the others later. For the electron density variation, we take

$$n_e(r, \theta) = n_0(r)(1 + \gamma(r)h(\theta)). \quad (5)$$

Since we consider the pedestal region, we can also take $\frac{\partial n_e}{\partial r} \gg \frac{1}{r} \frac{\partial n_e}{\partial \theta}$. With these assumptions the effect of the ion flow in the collision operator is merely to combine with the radial derivative of the electron density, which is taken at constant energy in eqn. (3), replacing it by the combination $\frac{\partial n_e}{\partial r} + \frac{T_i}{T_e} \frac{\partial n_i}{\partial r}$, (where we take the ion charge as $Z = 1$, so that quasi-neutrality requires $n_e = n_i$). The radial derivatives are of the actual densities as the electrostatic potential terms cancel between the ion and electron contributions (as in standard neoclassical theory). Thus, we have

$$\frac{v_{\parallel}}{Rq} \frac{\partial f_e}{\partial \theta} - \frac{m_e}{e} v_{\parallel} F_{Me} \frac{\partial}{\partial r} (\delta n(r, \theta)) \frac{\partial}{r \partial \theta} \left(\frac{v_{\parallel}}{B} \right) + C_e(f_e) + S(r, \theta, v) = 0 \quad (6)$$

with $\delta n = (1 + T_i/T_e)\delta n_e$. We take the source to be poloidally symmetric, in which case

$$S(r, v) = -\frac{m_e}{e} F_{Me} \left\langle \frac{\partial}{\partial r} (\delta n(r, \theta)) \frac{\partial}{r \partial \theta} \left(\frac{v_{\parallel}}{B} \right) \right\rangle / \left\langle \frac{1}{v_{\parallel}} \right\rangle. \quad (7)$$

297 4.2. The Incremental Bootstrap Current, δj_{bs} .

The lowest order solution f^0 is:

$$f^0 = \frac{m_e R q}{e} F_{Me} \left[\int_{\theta_0}^{\theta} d\theta \frac{\partial}{\partial r} (\delta n(r, \theta)) \frac{\partial}{r \partial \theta} \left(\frac{v_{\parallel}}{B} \right) - \int_{\theta_0}^{\theta} \frac{d\theta}{v_{\parallel}} \left\langle \frac{\partial}{\partial r} (\delta n(r, \theta)) \frac{\partial}{r \partial \theta} \left(\frac{v_{\parallel}}{B} \right) \right\rangle \frac{1}{\left\langle \frac{1}{v_{\parallel}} \right\rangle} \right] + g \quad (8)$$

where $\frac{\partial}{\partial \theta} g = 0$ and the end-point contribution from θ_0 to the integral (θ_0 is to be chosen judiciously to simplify calculations) can be absorbed into g . The function g is then determined from a solubility condition arising in first order in the collisional expansion:

$$\left\langle \frac{\partial}{\partial \lambda} \left(\frac{v_{\parallel} \lambda}{B} \frac{\partial}{\partial \lambda} f^0 \right) \right\rangle = 0, \quad (9)$$

where the operator $\langle A \rangle = \oint d\theta A / 2\pi$ for passing particles and $\langle A \rangle = \frac{1}{2} \Sigma_{\sigma} \int_{\theta_1}^{\theta_2} d\theta A / 2\pi$, with $v_{\parallel}(\theta_1) = v_{\parallel}(\theta_2) = 0$, for trapped particles. This determines $\frac{\partial g}{\partial \lambda}$ and hence $\frac{\partial f^0}{\partial \lambda}$. Now the

incremental bootstrap current is given by

$$\delta j_{bs} = -e \frac{\oint d\theta}{2\pi} \int d^3v v_{\parallel} f^0 = e\pi \langle \Sigma_{\sigma} \int Bd\lambda \int v_{\parallel} v^3 dv \lambda \partial f^0 / \partial \lambda / |v_{\parallel}| \rangle. \quad (10)$$

We then obtain

$$\delta j_{bs} = -\frac{3}{8} \frac{(T_e + T_i)}{B_{\theta}} \frac{d}{dr} (n_0(r) \gamma(r)) I, \quad (11)$$

where $I = (I_1 + I_2)$ with

$$I_1 = 2v \langle \int Bd\lambda B\lambda \left[\int_{\theta_0}^{\theta} d\theta h(\theta) \frac{\partial}{\partial \theta} \left(\frac{1}{v_{\parallel}} \right) - \frac{1}{\langle |v_{\parallel}| \rangle} \langle |v_{\parallel}| \int_{\theta_0}^{\theta} d\theta h(\theta) \frac{\partial}{\partial \theta} \left(\frac{1}{|v_{\parallel}|} \right) \rangle \right] \rangle, \quad (12)$$

$$I_2 = -2v \langle \int Bd\lambda B \frac{1}{\langle 1/|v_{\parallel}| \rangle} \left[\int_{\theta_0}^{\theta} d\theta \frac{1}{|v_{\parallel}|} - \frac{1}{\langle |v_{\parallel}| \rangle} \langle |v_{\parallel}| \int_{\theta_0}^{\theta} d\theta \frac{1}{|v_{\parallel}|} \rangle \right] \langle h(\theta) \frac{\partial}{\partial \theta} \left(\frac{1}{|v_{\parallel}|} \right) \rangle \rangle, \quad (13)$$

for passing particles, defined to be independent of v . For trapped particles, $I = I_3$ with

$$I_3 = 2v \langle \int Bd\lambda B \left[\langle \int_{\theta_0}^{\theta} d\theta h(\theta) \frac{\partial}{\partial \theta} \left(\frac{1}{|v_{\parallel}|} \right) - \int_{\theta_0}^{\theta} d\theta \frac{1}{|v_{\parallel}|} \frac{1}{\langle 1/|v_{\parallel}| \rangle} \rangle \langle h(\theta) \frac{\partial}{\partial \theta} \left(\frac{1}{|v_{\parallel}|} \right) \rangle \right] \rangle. \quad (14)$$

We can show that I_2 vanishes automatically, independently of $h(\theta)$. To evaluate the integral I over λ , we introduce

$$k^2 = 2 \frac{r}{R} \frac{\lambda B_0}{1 - \lambda B_0 (1 - \frac{r}{R})}; \quad v_{\parallel} = vu(\theta); \quad u = \sqrt{1 - k^2 \sin^2(\theta/2)} \quad (15)$$

298 Although $h(\theta)$ can be quite a general periodic function of θ , we first consider the two explicit
 299 cases: case (a), $h(\theta) = \cos \theta$ which is up-down symmetric; and case (b), $h(\theta) = \sin \theta$, which
 300 is in-out symmetric.

301 4.3. Case (a) $h(\theta) = \cos \theta$

302 We obtain

$$I = \frac{4}{\pi} \sqrt{\frac{2r}{R}} \int_0^1 \frac{k^2}{\left(\frac{2r}{R} + k^2 \left(1 - \frac{r}{R}\right)\right)^{5/2}} \left[\left(1 - \frac{2}{k^2}\right) K(k) - \frac{2}{k^2} E(k) - \frac{\pi^2}{2E(k)} \left(1 - \frac{2}{k^2}\right) \right] \\ + \frac{4}{\pi} \sqrt{\frac{2r}{R}} \int_0^{\infty} \frac{k^2}{\left(\frac{2r}{R} + k^2 \left(1 - \frac{r}{R}\right)\right)^{5/2}} \frac{1}{k} \left[\left(3 - \frac{4}{k^2}\right) K\left(\frac{1}{k}\right) - 2E\left(\frac{1}{k}\right) \right] \quad (16)$$

303 where K and E are the complete elliptic integrals of the first and second kind, respectively
 304 [38]. One can take the limit $r/R \rightarrow 0$ and still obtain a convergent integral.

While the first term requires numerical integration, yielding $-0.086\sqrt{(2r/R)}$, the second can again be calculated analytically using properties of the complete elliptic integrals [39], which yields $-20/9\pi\sqrt{(2r/R)} = -0.707\sqrt{(2r/R)}$. Consequently

$$\delta j_{bs} = 0.42 \sqrt{\frac{r}{R}} qR \frac{(T_e + T_i)}{B_0} \frac{d}{dr} (n_0(r) \gamma(r)). \quad (17)$$

305 4.4. Case (b): $h(\theta) = \sin \theta$

Here \hat{I}_1 vanishes exactly. The trapped region contribution also vanishes. Consequently, $j_{bs} = 0$ for case (b). Because \hat{I}_1 vanishes for $h(\theta) = \sin \theta$, a corollary is that for a sinusoidal variation of $h(\theta)$ centred on an arbitrary angle, $\theta = \beta$,

$$\delta j_{bs} = 2.54 \sqrt{\frac{r}{R}} q R \frac{(T_e + T_i)}{B_0} \frac{d}{dr} (n_0(r) \gamma(r)) \cos \beta. \quad (18)$$

306 4.5. Case (c): $h(\theta) = \delta(\theta - \alpha)$.

307 In this case we set $h(\theta) = \delta(\theta - \alpha)$, where α is the poloidal angle of the neutral influx, to
 308 calculate the incremental bootstrap current. We can calculate the integral I_1 in eqn. (12) for
 309 passing particles without difficulty. (The term arising from the azimuthal drift gives rise to
 310 derivatives of the δ -function, but these lie under double integrals and do not pose a problem,
 311 yielding a contribution which is in fact smaller than the one arising from the radial drift in
 312 the steep pedestal gradient.) However, employing the previous method is problematic for
 313 the trapped particle contribution. This is because the deeply trapped particles only respond
 314 to a limited range of pitch angles, depending on the angle α . The end-point contribution
 315 in the integration by parts in λ that arises from the maximum value of λ , λ_{Max} , which
 316 is no longer at $\lambda = \frac{1}{B_{Min}}$, does not vanish it is, in fact, singular, and is cancelled by a
 317 corresponding contribution from the integral term. It is therefore more convenient to calculate
 318 the contribution to the bootstrap current from trapped particles directly, as a straightforward
 319 integration over λ , rather than employing the integration by parts. This approach requires the
 320 distribution function g in the trapped region, which is a constant, and was not needed for the
 321 integration by parts method. In fact, $g = 0$ in the trapped region, to satisfy continuity at λ_{Max} .
 322 Of course, this needs to be accompanied by a boundary contribution evaluated at the trapped-
 323 passing boundary, to compensate for the integration by parts over passing particles which it
 324 is still convenient to retain. This boundary term dominates the integral one by a factor $1/2\epsilon$,
 325 as can be readily understood physically: while the trapped particle pitch angle integration
 326 over k introduces a factor $(2\epsilon)^{1/2}$, another from the trapped particle current, which involves
 327 the banana width, $\sim (2\epsilon)^{1/2}a$, and the typical trapped particle velocity $v_{\parallel} \sim (2\epsilon)^{1/2}v_{the}$ as
 328 a third. Thus, this contribution can be neglected, leaving to a simpler calculation of just the
 329 trapped passing boundary term, $I_b(\alpha)$. We define

$$G(\alpha, k) = \left[E - E\left(\frac{\alpha}{2}, k\right) / 2 \right], \quad 0 < \alpha < \pi, \quad (19)$$

$$G(\alpha, k) = E\left(\pi - \frac{\alpha}{2}, k\right) / 2, \quad \pi < \alpha < 2\pi, \quad (20)$$

with $E(\alpha/2, k)$ the incomplete elliptic integral of the second kind [38]. Thus

$$I_1(\alpha) = \sqrt{\frac{2r}{R}} \int_0^1 dk \frac{\sin \alpha}{(1 - k^2 \sin^2(\frac{\alpha}{2}))^{3/2}} \left[1 - \frac{\alpha}{2\pi} - \frac{G(\alpha, k)}{E(k)} \right] \quad (21)$$

$I_1(\alpha)$ is invariant under the substitution $\alpha \rightarrow 2\pi - \alpha$, so is symmetric about $\alpha = \pi$ (i.e., it is up-down symmetric, as is to be expected). There is also a contribution from the trapped region

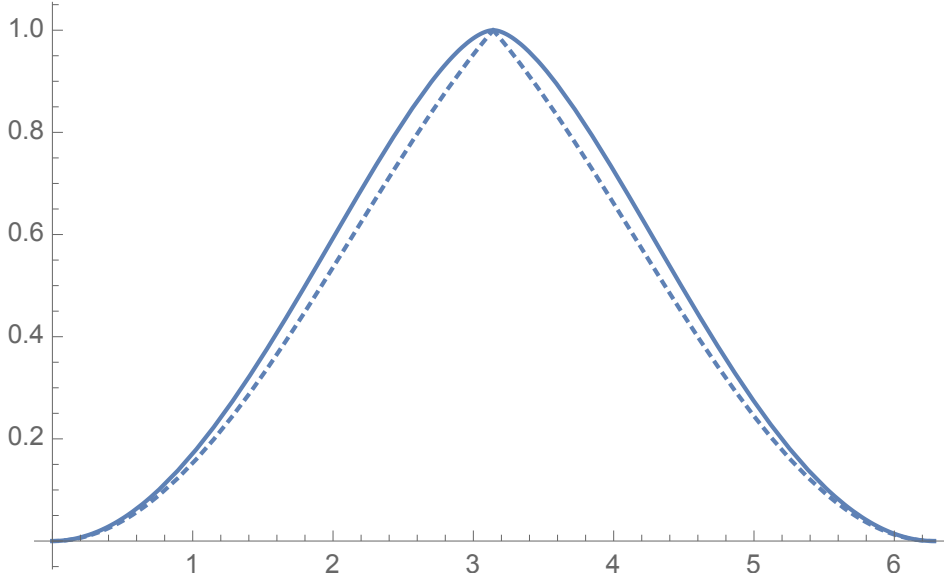


Figure 7. The variation with localisation angle, α , of the integral $\bar{I}(\alpha) = I(\alpha)/\sqrt{2r/R}$ for the δ -function, case (c). The dashed line is the dominant trapped particle contribution

and, as discussed above, this is dominated by the contribution from the flux-surface-averaged, trapped particle current density evaluated at the trapped - passing boundary. Calculating this from f^0 as given by eqn. (8) with $g = 0$, requires the evaluation of

$$I_b(\alpha) = 4\sqrt{\frac{2r}{R}} \left\langle \int_{\theta_0}^{\theta} d\theta \delta(\theta - \alpha) \frac{\partial}{\partial \theta} (u^{1/2}) - \frac{1}{\langle u^{-1/2} \rangle} \int_{\theta_0}^{\theta} d\theta u^{-1/2} \langle \delta(\theta - \alpha) \frac{\partial}{\partial \theta} (u^{1/2}) \rangle \right\rangle |_{k=1} \quad (22)$$

on the range $-\pi < \alpha < \pi$. this can be evaluated to yield

$$\hat{I}_b(\alpha) = -\frac{1}{2\pi} \sqrt{\frac{2r}{R}} \left[\theta_2 - \alpha - \frac{(\theta_2 + \theta_1)}{2} \right] = \frac{1}{\pi} \sqrt{\frac{2r}{R}} \sin(\alpha/2) \alpha, \quad (23)$$

since $\theta_2 = -\theta_1$; this contribution is also symmetric about $\alpha = \pi$, in the range $0 < \alpha < 2\pi$. Therefore, combining the result of a numerical evaluation of eqn. (21) and the analytic expression (23):

$$I(\alpha) = \sqrt{\frac{2r}{R}} \left[\int_0^1 dk \frac{(1 - \frac{\alpha}{2\pi} - \frac{G(\alpha, k)}{E(k)}) \sin \alpha}{(1 - k^2 \sin^2(\alpha/2))^{3/2}} + F(\alpha) \right], \quad (24)$$

$$F(\alpha) = \frac{1}{\pi} \alpha \sin\left(\frac{\alpha}{2}\right), \quad 0 < \alpha < \pi, \quad F(\alpha) = \frac{1}{\pi} (2\pi - \alpha) \sin\left(\frac{\alpha}{2}\right), \quad \pi < \alpha < 2\pi. \quad (25)$$

330 We notice that this remains finite at $\alpha = \pi$, the bounce point for just trapped particles, although
 331 the distribution function f^0 vanishes there; this is because the magnetic drift is singular there
 332 and the integration over θ with $h(\theta) = \delta(\theta - \alpha)$ remains finite in the limit $\alpha \rightarrow \pi$. (This can
 333 be seen more clearly by taking this limit after the integration the integration.)

A plot of $\bar{I}(\alpha) = I(\alpha)/\sqrt{(2r/R)}$ against α is shown in Fig. 7. $I(\alpha)$ vanishes at $\alpha = 0$ and 2π , peaking at $\alpha = \pi$; in between it spans the range $0 < I(\alpha) < \sqrt{(2r/R)}$. Finally, we have

$$\delta j_{bs} = \frac{3}{8} \frac{(T_e + T_i)}{B_\theta} \frac{d}{dr} (n_0(r) \gamma(r)) I(\alpha). \quad (26)$$

334 Although this result is itself significant, the bootstrap current response to the δ -function
 335 source also provides a Green's function for a general poloidal density perturbation specified
 336 by $\gamma(r)h(\theta)$.

337 4.6. Green's Function

A consequence of modifying the approach to calculating the bootstrap current that we adopted in the case of the δ -function source was that calculating the trapped particle contribution could be achieved more simply for a general $h(\theta)$ by just considering the trapped particle current density at the trapped-passing boundary, rather than requiring an integration over trapped values of k . Thus, both passing and trapped contributions involve integrations over the full range of θ : $0 < \theta < 2\pi$, rather than the limited range sampled by the trapped particles. This facilitates the demonstration of a Green's function approach based on our solution for the δ -function case, since, as we shall see, the integrations over α and δ that are involved, commute, so one can readily change the orders of these integrations. Thus, we see that the δ -function source provides a Green's function for a poloidal density perturbation specified by $h(\theta) = \delta(\theta - \alpha)$, where we utilise the replacement

$$h(\theta) \rightarrow \oint d\alpha h(\alpha) \quad (27)$$

338 in eqns. (12), (13) and (14).

339 4.7. General axisymmetric, toroidal geometry.

We introduce an axisymmetric toroidal co-ordinate system, ψ, θ, ϕ , where ψ is the poloidal flux, θ is a poloidal angle such that the magnetic field lines are straight, and ϕ is the toroidal angle. The magnetic field is given by

$$B = I(\psi) \nabla \phi + \nabla \phi \times \nabla \psi, \quad (28)$$

340 We now define the operator $\langle \rangle$ by $\langle A \rangle = \oint R^2 d\theta A / \oint R^2 d\theta$. Because of these relations, the
 341 solution for f^0 , given in eqn. (8), still pertains, provided we use the new definition for $\langle \rangle$,
 342 as does the solution for g . From the current continuity equation $\nabla \cdot j = 0$, it follows that
 343 the appropriate object to consider in general geometry is the flux-surface average quantity
 344 $\langle \delta j_{bs} / B \rangle$ and we obtain

$$\left\langle \frac{\delta j_{bs}}{B} \right\rangle = -\frac{3}{8} \frac{I(T_e + T_i)}{qB_{Max}} \frac{d}{d\psi} (n_0(\psi) \gamma(\psi, \theta)) I, \quad (29)$$

We follow a parallel set of steps to those used for the large aspect case to obtain a passing contribution

$$I(\alpha) = 2\nu B_{Max} \frac{\partial}{\partial \alpha} \left(\frac{1}{|v_{\parallel}|} \left[\frac{\int_{\alpha}^{2\pi} d\theta R^2}{\oint d\theta R^2} - \frac{\int_{\alpha}^{2\pi} d\theta R^2 |v_{\parallel}|}{\oint d\theta R^2 |v_{\parallel}|} \right] \right). \quad (30)$$

For the trapped contribution we find

$$I(\alpha) = F(\alpha) = 4 \frac{B_{Max}}{\nu} \frac{\partial}{\partial \alpha} \left(\frac{v_{\parallel}}{B} \right) \Big|_{\lambda=B_{Max}} \left[\frac{\int_{\alpha}^{2\pi} d\theta R^2}{\oint d\theta R^2} \right], \quad 0 < \alpha < \pi, \quad (31)$$

$$I(\alpha) = F(2\pi - \alpha), \quad \pi < \alpha < 2\pi. \quad (32)$$

345 In the following section we need to extend the collision model to include electron-electron
 346 collisions, but this is only completely justified in the limit of a small number of trapped
 347 particles, so the general equilibria discussed above are then constrained to satisfy this
 348 condition.

349 4.8. The effect of a poloidal variation in the temperature

If the perturbed pressure is to vanish on a flux surface as required by MHD equilibrium, then

$$\delta p = (T_e + T_i) \delta n + n_0 (\delta T_e + \delta T_i) = 0 \quad (33)$$

assuming quasi-neutrality. We also assume equipartition between ion and electron temperatures,

$$T_i = T_e, \quad \delta T_e = \delta T_i \equiv \delta T, \quad \text{so} \quad \delta T = \frac{\delta n}{n_0} T_e. \quad (34)$$

Alternatively, rapid parallel electron thermal transport removes the electron temperature perturbation requiring the ion temperature perturbation to facilitate pressure balance, when

$$\delta T_e = 0; \quad \delta T_i = (T_e + T_i) \frac{\delta n}{n_0} \quad (35)$$

If the plasma density source is sufficient to prevent equalisation of pressure a more complex equilibrium must be considered. The analogous results to those for the large aspect ratio case will be equivalent to those for the usual calculation of the bootstrap current driven by equilibrium gradients across constant density flux surfaces with a Lorentz collision operator, apart from the effect of the geometrical factor I . The same situation will be true if we consider the effects of δT with like-particle collisions and energy-dependent collision frequencies, when we can exploit the corresponding results given in Ref. [37]. These calculations give

$$j_{bs} = -1.46 \left(\frac{r}{R} \right)^{1/2} \frac{n_0 T_e}{B_{\theta}} \left[\left(1 + \frac{T_i}{T_e} \right) \frac{1}{n_0} \frac{dn_e}{dr} + \frac{1}{T_e} \frac{dT_e}{dr} - \frac{0.17}{T_e} \frac{dT_i}{dr} \right] \quad (36)$$

for the Lorentz model and

$$j_{bs} = -1.46 \left(\frac{r}{R} \right)^{1/2} \frac{n_0 T_e}{B_{\theta}} \left[1.66 \left(1 + \frac{T_i}{T_e} \right) \frac{1}{n_0} \frac{dn_e}{dr} + \frac{0.47}{T_e} \frac{dT_e}{dr} - \frac{0.29}{T_e} \frac{dT_i}{dr} \right] \quad (37)$$

when electron-electron collisions and the energy dependence of the collisions are included. Now the effective density gradient term in the case of the Lorentz collision model must be multiplied by a factor 1.66 and expressions (33) and (34) or (35) used for the temperature gradient contributions. Thus, in the first case for example, we obtain

$$\delta j_{bs} = 2.36 \frac{n_0 T_e}{B_\theta} \left(1 + \frac{T_i}{T_e} \right) \frac{1}{n_0} \frac{dn_0}{dr} \gamma I \quad (38)$$

350 where we note $I = -\sqrt{(2r/R)}c$, with the constant c depending on the function $h(\theta)$
 351 describing the poloidal variation of the plasma density.

352 4.9. Conclusions

353 We have investigated the effect of poloidal variations of the plasma density, $\delta n = \gamma h(\theta)n_0$,
 354 on the bootstrap current in a large aspect ratio tokamak equilibrium, such as might arise
 355 in gas-puffing experiments, recycling neutral influxes or as a result of toroidal rotation.
 356 The calculation has assumed that the lowest order distribution function is Maxwellian for
 357 simplicity, although it may be distorted from a simple Maxwellian in reality. A more realistic
 358 distribution function might produce additional effects on the bootstrap current, but it would be
 359 much more difficult to obtain this function and calculate the consequences. The effect of the
 360 poloidal temperature variations resulting from this density variation has also been addressed,
 361 as has the generalisation to an arbitrary axisymmetric toroidal geometry. Three explicit cases
 362 for the density variation have been considered: case (a) which is sinusoidal and up-down
 363 symmetric and is also relevant to the effect of toroidal rotation; case (b) which is sinusoidal
 364 and symmetric in the inboard-outboard direction (the effect of sinusoidal symmetry about any
 365 other poloidal angle could be deduced simply from decomposing it into a combination of the
 366 cases (a) and (b)), and case (c) which is a very localised poloidal variation, approximated by
 367 a δ -function in poloidal angle. In case (b) we find the incremental current vanishes exactly,
 368 while for case (c) the results naturally depend on the poloidal angle α , describing the location
 369 of the neutral influx. We find that the largest effect in this case does occur for localisations
 370 near the inboard side of the plasma column. Whether and by how much the bootstrap current
 371 increases or decreases depends on both the magnitude and sign of an integral, I , specific to
 372 each poloidal density variation, $h(\theta)$, and the amplitude and sign γ , of this variation.

373 The result for case (c) also serves as a Green's function for calculating the bootstrap
 374 current response to an arbitrary poloidal distribution for the density perturbation numerically
 375 by a simple quadrature; it also clearly demonstrates why the current vanishes in case (b), or
 376 indeed in any up-down symmetric case. Furthermore, it facilitates the treatment of a general,
 377 axisymmetric toroidal geometry, albeit requiring there to be only a small number of trapped
 378 particles to justify the use of the simple pitch-angle collision operator. We also limit ourselves
 379 to up-down symmetric equilibria to simplify the calculation. Although we employed a Lorentz
 380 collision operator, appropriate to electron-ion collisions, we demonstrate that our results can
 381 be readily adapted to allow for the effects of electron-electron collisions, energy-dependent
 382 collisions and the poloidally varying electron and ion temperature perturbations, $\delta T_{e,i}(\theta)$, that

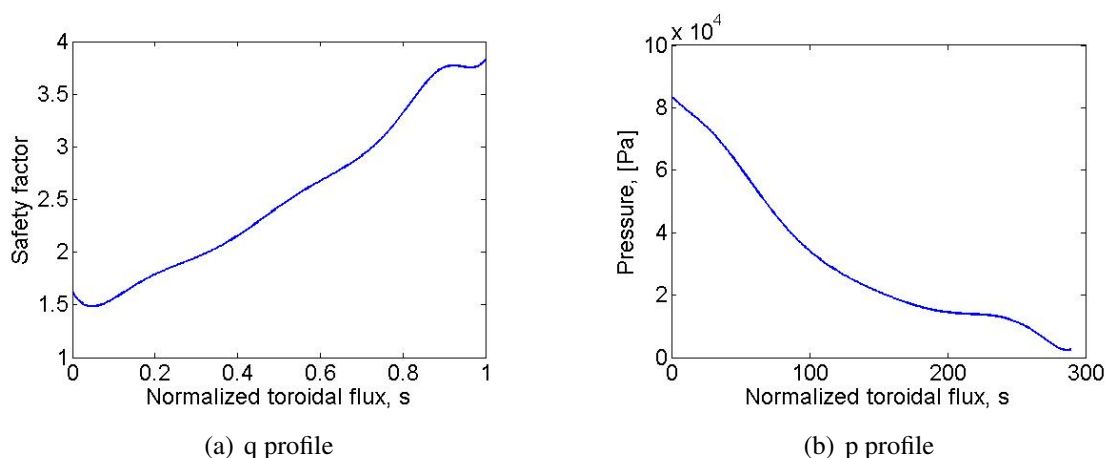


Figure 8. Pressure and safety factor profiles for the current driven mode.

383 would ensure pressure remains constant on a flux surface (and restores the usual poloidally
 384 varying Pfirsch-Schluter current as a consequence).

385 One can expect this poloidal density variation to be linked to the location of any neutral
 386 influx or, perhaps, gas-puffing. Thus, an up-down symmetric case may be related to case (a),
 387 while symmetric vertical locations near upper and lower X-points may relate to case (b). Case
 388 (c) appears to provide a good representation of the results of gas-puffing experiments

389 The differences in the magnitude and sign of the incremental bootstrap current caused by
 390 the nature of the poloidal density variations may have implications for Type 1 ELMs and their
 391 control, since their onset is believed to be triggered when peeling-ballooning modes, whose
 392 stability is affected by edge plasma currents, become unstable.

393 5. QH mode

394 5.1. VMEC equilibrium modelling

395 Candidate modes which may explain the QH-mode are investigated using the VMEC [40]
 396 non-axisymmetric equilibrium code and the linear ballooning stability code COBRAVMEC
 397 [41, 42]. Previous work has investigated how such a saturated MHD mode may appear at the
 398 plasma edge [15]. It has been shown that such a mode can appear due to the q profile being
 399 just below a rational value at the plasma edge. This is the external kink mode, see Fig. 8(a)
 400 showing the q profile. VMEC models the plasma as a current carrying plasma column with
 401 a vacuum region outside. This allows the q value at the plasma edge to be well defined. In
 402 reality these are diverted plasmas and so formally the q will go to infinity at the plasma edge.
 403 This would mean that external kink modes are unlikely to form. However, error fields and
 404 other non-axisymmetric fields may well create a stochastic layer at the plasma edge so that
 405 there is a maximum edge q . An improved understanding of the physics of the separatrix and
 406 external kink modes is required.

407 A saturated MHD mode can also appear as a result of a pressure driven mode and a

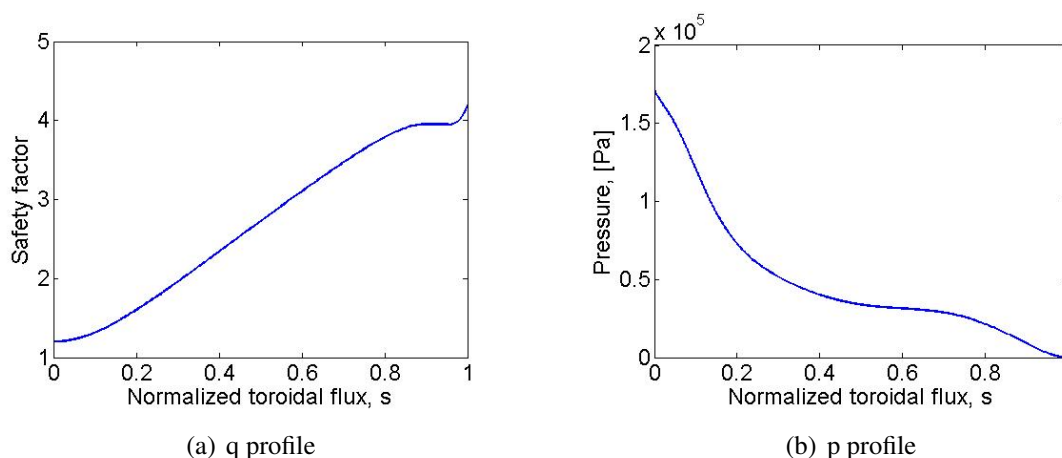


Figure 9. Pressure and safety factor profiles for the pressure driven mode.

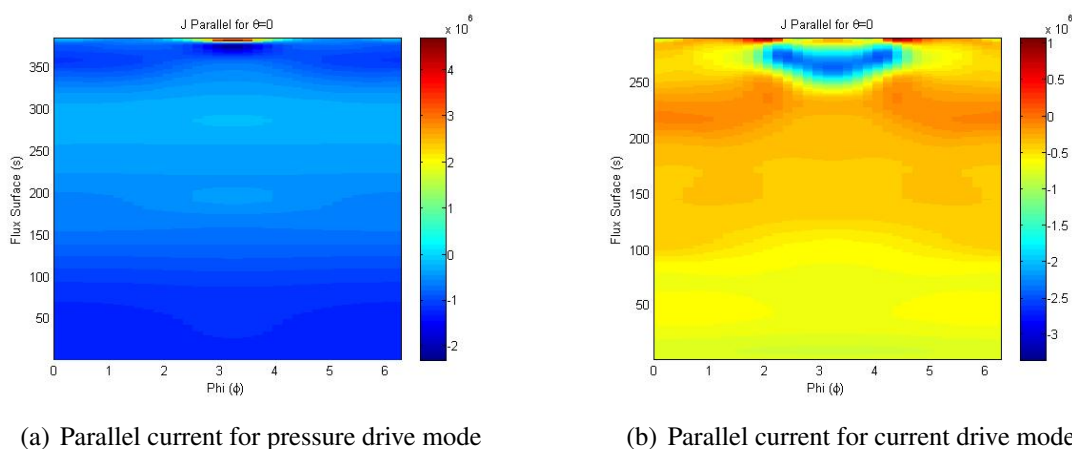
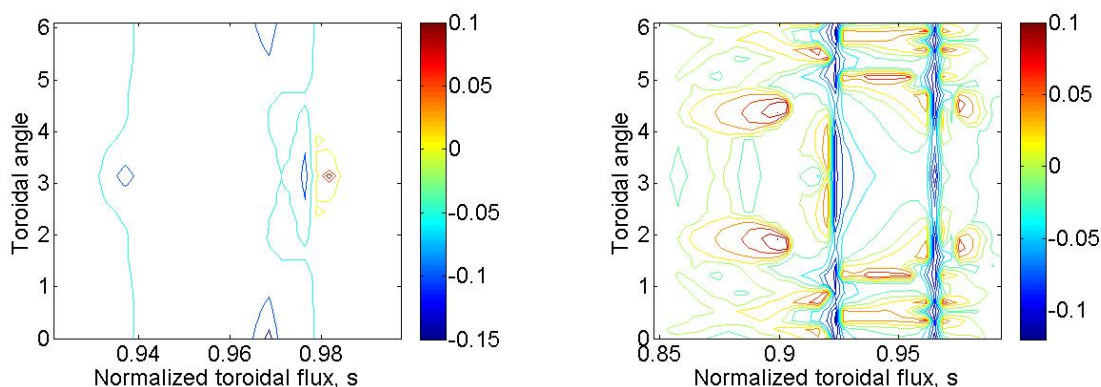


Figure 10. Parallel current for the current and pressure driven modes. A much broader current ribbon appears for the current driven mode than for the pressure driven mode.

408 flattening of the q profile which is caused by the bootstrap current, see figure 9(a) showing the
 409 q profile for this mode. Note that the q profile is above four at the edge which removes drive for
 410 the current driven mode. We call this second type of mode the external mode (after Brunetti
 411 [43]). We expect this pressure driven mode to appear at low collisionality as it requires a
 412 significant bootstrap current to flatten the q profile at the edge.

413 We investigate the differences between the external kink mode and the external mode to
 414 help to understand which of these modes we see experimentally. It has been noted by Solano
 415 et al [13] that in JET a current ribbon appears at the plasma edge. We have processed the
 416 external kink mode and external mode equilibria to see if a current ribbon is in evidence.
 417 Figure 10 shows the parallel current for the external kink mode and the external mode. We
 418 see that the external kink mode has a current ribbon in the pedestal region while the external
 419 mode only has a current perturbation at the very edge of the plasma.



(a) Ballooning mode growth rate for the pressure driven mode

(b) Ballooning mode growth rate for the current driven mode

Figure 11. Linear ballooning mode growth rates for the external kink and pressure driven modes.

420 5.2. Linear ballooning stability

421 We now investigate the local linear ballooning stability using the COBRAVMEC code. This
 422 calculates the growth rate of the local ballooning mode on a given fieldline. It can also be
 423 thought of as the infinite- n ballooning mode. This is of interest because it captures some of
 424 the instability drive of the kinetic ballooning mode (KBM). The KBM is thought to drive
 425 particle transport, rather than heat transport, which is an important element of the QH-mode
 426 [44]. We first calculated ballooning stability for axisymmetric sister equilibria for the cases
 427 that are unstable to external kink mode and external mode. Ballooning modes are found to
 428 be stable to these axisymmetric equilibria. In contrast, for the 3D equilibria corresponding to
 429 the external kink saturated state, strong ballooning instability is found over a large fraction of
 430 the edge region, see Fig. 11. The 3D equilibria corresponding to the external mode saturated
 431 state is only weakly unstable to ballooning modes, and only very near the edge. Ideal MHD
 432 infinite n ballooning instability in the external kinked 3D equilibria could imply ballooning
 433 related, or KBM related, density transport

434 This result may have been expected since it is well known from the physics of resonant
 435 magnetic perturbation (RMP) ELM suppression and mitigation that density pump out is only
 436 seen when the plasma response is external kink like (i.e. largest around the X-point) rather
 437 than ballooning-like [45](where ballooning-like in this context means pressure driven external
 438 like). In RMP cases we would not expect to see the current ribbon at the plasma edge as this
 439 effectively comes from the coils around the plasma.

440 5.3. Conclusions

441 We examined two types of MHD mode which can produce saturated free boundary states: an
 442 external kink mode and a pressure driven, external, mode. We have shown that the external
 443 kink mode produces a perturbed current ribbon at the plasma edge in line with experimental

444 observations. We have also calculated the linear local ballooning stability of these saturated
445 modes. The external kink mode significantly destabilizes the ballooning modes while the
446 pressure driven mode does not. This result matches expectations from the results of RMP
447 ELM control experiments which show that density pump out only occurs for plasmas with
448 an external kink mode response. The hypothesis is that the KBM produces sufficient partial
449 transport such that the pedestal never reaches the peeling ballooning boundary and so no
450 ELMs occur.

451 **6. Summary and Directions for future work**

452 We have completed various strands of work to improve our understanding of reactor relevant
453 pedestals. While we have some understanding of what sets the pedestal height and width
454 there is still much to understand. We have investigated how to improve the EPED model by
455 trying to remove assumptions about the density. We have tried to determine if a gyrokinetic
456 calculation of the heat flux could help us to determine the density profile. Unfortunately, the
457 linear gyrokinetic results (and probably the nonlinear results too) are not able to discriminate
458 between differing pairs of density and temperature profiles. We believe that this comes from
459 the pedestal transport criterion assumed in EPED. This assumption should be relaxed in future
460 work. It has been observed that density is not a flux surface function in many plasmas
461 due to, for example, plasma rotation or plasma fuelling. We have calculated the effect of
462 non flux surface density on the bootstrap current analytically in this paper and numerical
463 investigations using ELMFIRE have also been completed [9]. This changed bootstrap current
464 will also change the stability of the peeling ballooning modes and thus the ELM stability. We
465 have calculated the effect of non flux surface density using JOREK within the project. This
466 indicated that the low n modes became more unstable and the high n modes were unaffected.
467 This was preliminary work and further confidence in the equilibrium is needed before this can
468 be regarded as a final result. Indeed improving our understanding and measurements of the
469 bootstrap current is still an important topic of research. The effect of plasma turbulence on
470 the bootstrap current is yet to be determined and will require a code such as ELMFIRE to be
471 resolved.

472 Type I ELMs will not be allowable in reactors due to the damage they will cause to
473 plasma facing components. We will therefore need to develop our confidence in small and
474 no ELM regimes. We investigated the QH-mode using the non-axisymmetric equilibrium
475 code VMEC. In this paper we built on work looking at current and pressure driven modes.
476 Linear ballooning stability analysis indicates that the QH-mode is a saturated external kink
477 mode rather than a pressure driven mode. A gyrokinetic analysis of these equilibria would
478 allow us to understand the effect on transport of non-axisymmetric saturated instabilities.
479 This would also be an important step in understanding RMP ELM control experiments. Work
480 was carried out on other small ELM regimes within this collaboration which will be reported
481 elsewhere. There are lots of avenue for further work including use of the gyro-landau-fluid
482 model implemented in BOUT++ to model I-mode.

483 A final aspect of this collaboration is the use of neural networks to produce fast surrogate

484 models. This will be important if we hope to use these models to design reactors and to scan
485 large regions of parameter space for favourable reactor relevant conditions.

486 Acknowledgements

487 This work resulted from a collaboration under the EUROfusion Enabling Research grant on
488 Reactor Relevant Pedestals (ENR-MFE19.CCFE-04-T002-D001). This work was supported
489 in part by the Swiss National Science Foundation. CJH would like to acknowledge the work
490 of Samuli Saarelma who was the original PI for this project. CJH also wishes to thank
491 B Chapman who was the primary originator of Section 3 and J W Connor who produced
492 Section 4. JWC would like to acknowledge Jim Hastie, Per Helander, Howard Wilson and
493 James Simpson for their thoughts and comments. BC would like to acknowledge Lorenzo
494 Frassinetti for preparation of the JET profile and useful discussions.

495 This work has been carried out within the framework of the EUROfusion Consortium
496 and has received funding from the Euratom research and training programme 2014-2018
497 and 2019-2020 under grant agreement No 633053 and from the RCUK [grant number
498 EP/T012250/1]. To obtain further information on the data and models underlying this paper
499 please contact PublicationsManager@ukaea.uk. The views and opinions expressed herein do
500 not necessarily reflect those of the European Commission.

501 References

- 502 [1] C.J. Ham, A. Kirk, S. Pamela, and H. Wilson. Filamentary plasma eruptions and their control on the route
503 to fusion energy. *Nature Reviews Physics*, 2(3):159–167, 2020.
- 504 [2] P. B. Snyder *et al* . A first-principles predictive model of the pedestal height and width: development,
505 testing and iter optimization with the eped model. *Nucl. Fusion*, 51:103016, 2011.
- 506 [3] S. Saarelma *et al* . Self-consistent pedestal prediction for JET-ILW in preparation of the DT campaign.
507 *Physics of Plasmas*, 26:072501, 2019.
- 508 [4] E Belli and J Candy. Kinetic calculation of neoclassical transport including self-consistent electron and
509 impurity dynamics. *Plasma Phys. Control. Fusion*, 50:095010, 2008.
- 510 [5] E Belli and J Candy. Full linearized fokkerplanck collisions in neoclassical transport simulations. *Plasma*
511 *Phys. Control. Fusion*, 54:015015, 2012.
- 512 [6] O. Sauter *et al* . Neoclassical conductivity and bootstrap current formulas for general axisymmetric
513 equilibria and arbitrary collisionality regime. *Physics of Plasmas*, 6:2834, 1999.
- 514 [7] R. Hager *et al* . Bootstrap formula. *Physics of Plasmas*, 23:042503, 2016.
- 515 [8] J. A. Heikkinen *et al* . Elmfire. *Journal of Computational Physics*, 227:5582, 2008.
- 516 [9] T .Kiviniemi *et al* . Simulating the effect of poloidal particle source on the bootstrap current in tokamak
517 edge pedestal. *Plasma Physics and Controlled Fusion*, in preparation, 2021.
- 518 [10] G. Huysmans and O. Czarny. MHD stability in X-point geometry: simulation of ELMs. *Nuclear Fusion*,
519 47:659, 2007.
- 520 [11] A Gillgren and P Strand. PENN for JET. *in preparation*, 2021.
- 521 [12] K.H. Burrell *et al* . Discovery of stationary operation of quiescent h-mode plasmas with net-zero neutral
522 beam injection torque and high energy confinement on DIII-D. *Phys. Plasmas*, 23:056103, 2016.
- 523 [13] E.R. Solano *et al* . Observation of confined current ribbon in JET plasmas. *Phys. Rev. Lett.*, 104:185003,
524 2010.
- 525 [14] W. Suttrop *et al* . Elm-free stationary h-mode plasmas in the asdex upgrade tokamak. *Plasma Phys. Control.*
526 *Fusion*, 45:1399, 2003.

- 527 [15] A. Kleiner. Non-linear modelling of saturated internal and external MHD instabilities in tokamaks. *PhD*
528 *Thesis EPFL Switzerland*, 2019.
- 529 [16] D. Brunetti. JET QH-mode. *in preparation*, 2021.
- 530 [17] D. Brunetti. Type III ELMs. *in preparation*, 2021.
- 531 [18] C. Bourdelle, X. Garbet, F. Imbeaux, A. Casati, N. Dubuit, R. Guirlet, and T. Parisot. A new gyrokinetic
532 quasilinear transport model applied to particle transport in tokamak plasmas. *Physics of Plasmas*,
533 14(11):112501, 2007.
- 534 [19] L Horvath et al. Isotope dependence of the type I ELMy H-mode pedestal in JET-ILW hydrogen and
535 deuterium plasmas. *Nuclear Fusion*, 61:046015, 2021.
- 536 [20] F. Jenko, W. Dorland, M. Kotschenreuther, and B. N. Rogers. Electron temperature gradient driven
537 turbulence. *Physics of Plasmas*, 7(5):1904–1910, 2000.
- 538 [21] T. Görler, X. Lapillonne, S. Brunner, T. Dannert, F. Jenko, F. Merz, and D. Told”. The global version of
539 the gyrokinetic turbulence code gene. *Journal of Computational Physics*, 230(18):7053 – 7071, 2011.
- 540 [22] J Simpson et al. Using EDGE2D-EIRENE to simulate the effect of impurity seeding and fueling on the
541 upstream electron separatrix temperature. *Nuclear Materials and Energy*, 20:100599, 2019.
- 542 [23] L. Frassinetti, M.G. Dunne, U. Sheikh, S. Saarelma, C.M. Roach, E. Stefanikova, C. Maggi, L. Horvath,
543 S. Pamela, E. de la Luna, E. Wolfrum, M. Bernert, P. Blanchard, B. Labit, A. Merle, L. Guimaraes,
544 S. Coda, H. Meyer, and J.C. Hillesheim. Role of the pedestal position on the pedestal performance in
545 AUG, JET-ILW and TCV and implications for ITER. *Nuclear Fusion*, 59(7):076038, 2019.
- 546 [24] S. Saarelma, L. Frassinetti, P. Bilkova, C. D. Challis, A. Chankin, R. Fridstrm, L. Garzotti, L. Horvath, and
547 C. F. Maggi. Self-consistent pedestal prediction for jet-ilw in preparation of the dt campaign. *Physics*
548 *of Plasmas*, 26(7):072501, 2019.
- 549 [25] M.G. Dunne et al. The role of the density profile in the asdex-upgrade pedestal structure. *Plasma Phys.*
550 *Control. Fusion*, 59:014017, 2017.
- 551 [26] D.R. Hatch, M. Kotschenreuther, S. Mahajan, P. Valanju, and X. Liu. A gyrokinetic perspective on the
552 JET-ILW pedestal. *Nuclear Fusion*, 57(3):036020, 2017.
- 553 [27] D.R. Hatch, M. Kotschenreuther, S.M. Mahajan, G. Merlo, A.R. Field, C. Giroud, J.C. Hillesheim, C.F.
554 Maggi, C. Perez von Thun, C.M. Roach, and S. Saarelma and. Direct gyrokinetic comparison of pedestal
555 transport in JET with carbon and ITER-like walls. *Nuclear Fusion*, 59(8):086056, 2019.
- 556 [28] T. Luda, C. Angioni, M.G. Dunne, E. Fable, A. Kallenbach, N. Bonanomi, P.A. Schneider, M. Siccinio,
557 G. Tardini, and and. Integrated modeling of ASDEX upgrade plasmas combining core, pedestal and
558 scrape-off layer physics. *Nuclear Fusion*, 60(3):036023, 2020.
- 559 [29] D. Moulton, B. Lipschultz, and J. Harrison. X. *EPS Conference*, 44th EPS Conf. on Plasma Physics,
560 Belfast, June 26-30, paper(X):O6.129., 2017.
- 561 [30] R.J. Bickerton, J.W. Connor, and J.B. Taylor. *Nature Physical Science*, 229:110, 1971.
- 562 [31] J.W. Connor, R.J. Hastie, H.R. Wilson, and R.L. Miller. Magnetohydrodynamic stability of tokamak edge
563 plasmas. *Physics of Plasmas*, 5:2687, 1998.
- 564 [32] J.A. Wesson. X. *Nuclear Fusion*, 37(X):571, 1977.
- 565 [33] P. Helander, T. Fulop, and M. Lisak. Tokamak current driven by poloidally asymmetric fueling. *Physics*
566 *of Plasmas*, 13:102506, 2006.
- 567 [34] J. Simpson. X. *Private communication*, (X), 2020.
- 568 [35] E.R. Solano and R.D. Hazeltine. Effect of asymmetric sources on tokamak neoclassical transport in the
569 plateau regime. *Phys. Fluids B*, 2(9):2113, 1990.
- 570 [36] M. N. Rosenbluth, P.H. Rutherford, J. B. Taylor, E. A. Frieman, and L. M. Kovrizhnykh. *Plasma Phys.*
571 *Controlled Nuclear Fusion Research*, 1:495, 1971.
- 572 [37] P. Helander and D.J. Sigmar. Collisional transport in magnetized plasmas. *Cambridge University Press*,
573 (X), 2002.
- 574 [38] M. Abramowitz and Stegun. Handbook of mathematical functions. (*New York: National Bureau of*
575 *Standards, Applied Mathematics*), page Chapter 19, 1972.
- 576 [39] Erdelyi. Higher transcendental functions. (*McGraw-Hill Book Company inc., New York, Vol. II.*, page
577 chapter XIII, 1953.

- 578 [40] S. Hirshman and J. C. Whitson. Steepestdescent moment method for threedimensional magnetohydrody-
579 namic equilibria. *Phys. Fluids*, 26:3553, 1983.
- 580 [41] R Sanchez et al. COBRA: an optimized code for fast analysis of ideal ballooning stability of three-
581 dimensional magnetic equilibria. *J. Comput. Phys.*, 161:576, 2000.
- 582 [42] R Sanchez et al. COBRAVMEC. *Comput. Phys. Commun.*, 135:82, 2001.
- 583 [43] D. Brunetti, J.P. Graves, E. Lazzaro, A. Mariani, S. Nowak, W.A. Cooper, and C. Wahlberg. Excitation
584 mechanism of low- n edge harmonic oscillations in edge localized mode-free, high performance, tokamak
585 plasmas. *Phys. Rev. Lett.*, 122:155003, 2019.
- 586 [44] M. Kotschenreuther et al. *Nucl. Fusion*, 59:096001, 2019.
- 587 [45] Yueqiang Liu, C.J. Ham, A. Kirk, Li Li, A. Loarte, D.A. Ryan, Youwen Sun, W. Suttrop, Xu Yang, and
588 Lina Zhou. ELM control with RMP: plasma response models and the role of edge peeling response.
589 *Plasma Phys. Control. Fusion*, 58(X):114005, 2016.